ARTICLE

Multiparametric Modulation of Magnetic Transduction for Biomolecular Sensing in Liquids

Received 00th January 20xx,
Accepted 00th January 20xx

DOI: 10.1039/x0xx00000x

Elena Sanz-de Diego,[a] Antonio Aires,[b] Pablo Palacios-Alonso,[a] David Cabrera,[a,c] Niccolo Silvestri,[d] Cinthia C. Vequi-Suplicy,[a] Emilio J. Artés-Ibáñez,[a,e] José Requejo-Isidro,[f,g] Rafael Delgado-Buscalioni,[h] Teresa Pellegrino,[d] Aitziber L.Cortajarena,[*a,b,i] and Francisco J. Terán[*a,e,g]

Recent COVID19 pandemic has remarkably boosted the research on *in vitro* diagnosis assays to detect biomarkers in biological fluids. Specificity and sensitivity are mandatory for diagnostic kits aiming to reach clinical stages. Whilst the modulation of the sensitivity can significantly improve the detection of biomarkers in liquids, this has been scarcely explored. Here, we report on the proof of concept, and parametrization of a novel biosensing methodology based on the changes of AC magnetic hysteresis area observed for magnetic nanoparticles following biomolecular recognition in liquids. Several parameters are shown to signficantly modulate the transducing capacity of magnetic nanoparticles to detect analytes dispersed in saline buffer at concentrations of clinical significance. Magnetic nanoparticles were bio-conjugated with an engineered recognition peptide as receptor. Analytes are engineered tetratricopeptide binding domains fused to the fluorescent protein whose dimerization state allows mono- or di-valent variants. Our results unveil that the number of receptors per particle, analyte valency and concentration, nanoparticle composition and concentration, and field conditions play a key role on the formation of assemblies driven by biomolecular recognition. Consequently, all these parameters modulate the nanoparticle transduction capacity. Our study provides essential insights on the potential of AC magnetometry for customizing biomarker detection in liquids.

Introduction

COVID19 pandemic has triggered the research on nanotechnology[1] to achieve user-friendly, quick, and accurate *in vitro* diagnosis assays for detection of analytes (i.e., biomarkers, antigens, or pathogens) linked to physiological or pathogenic states. [2] Specificity and sensitivity are mandatory features to be accomplished by *in vitro* diagnostic tests aiming to reach clinical use.[3] While specificity is exclusively linked to biological elements -named receptors- involved in the biomolecular recognition of analytes, sensitivity is associated with the receptor-analyte affinity and the transduction element employed to label the receptor-analyte recognition. Generally, the capacity to modulate the detection sensitivity on current sensing methodologies is rather limited, and generally associated with the signal/noise ratio of the physical measurements displayed by the transducer. Interestingly, transduction methodologies supplying multiparametric sensitivity gain in versatility to adequate biomarker detection in liquids to the experimental circumstances (i.e., biomarker concentration).[4] Recent progress in nanoscience and nanotechnology offers novel transducing potential such as, photoelectrochemical,[5,6] optical,[7,8] colorimetric[9–11], photothermal,[12] or magnetic[13,14] signals. Indeed, nanoscale transducers have witnessed a great attention thanks to their ability to detect biomarkers in biological fluids at concentrations of clinical significance.[15,16] In general, the physical fundamentals related to nanoparticle transduction benefits from its final colloidal state. While the number of reported methodologies[7,8] involving individual nanoparticles to display analyte recognition phenomena is limited, many others take advantage from nanoparticle aggregation[9,10,12,17–22]. More research is needed on detection methodologies based on nanoparticles, whose sensitivity can be tuned by multiple parameters. This is the case for magnetic nanoparticles (MNPs),[23] which have shown great potential as sensing transducers.[14,24] Different experimental techniques[20,22,25–29] such as magneto-resistance, AC magnetic susceptometry,

[a] iMdea Nanociencia, Ciudad Universitaria de Cantoblanco, 28049 Madrid, Spain
[b] CIC biomaGUNE, Basque Research and Technology Alliance (BRTA). Paseo de Miramón 194, 20014, Donostia-San Sebastián, Spain
[c] School of Pharmacy and Bioengineering, Keele University, Guy Hilton Research Centre, Thurnburrow Drive, ST4 7QB, Stoke on Trent, UK
[d] Istituto Italiano di Tecnologia, Via Morego 30, 16163, Genoa, Italy
[e] Nanotech Solutions, 40150 Villacastín, Spain
f Centro Nacional de Biotecnologia (CSIC), 28049 Madrid, Spain
[g] Nanobiotecnología (iMdea-Nanociencia), Unidad Asociada al Centro Nacional de Biotecnología (CSIC), 28049 Madrid, Spain
[h] Dpto Física Teórica Materia Condensada, Universidad Autónoma de Madrid, 28049 Madrid, Spain
[i] Ikerbasque, Basque Foundation for Science, Bilbao, Spain
E-mail :francisco.teran@imdea.org; alcortajarena@cicbiomagune.es
Electronic Supplementary Information (ESI) available. See DOI: 10.1039/x0xx00000x

magnetic particle spectroscopy, or relaxivity display changes of MNP magnetic properties after specific interaction with analytes. Such magnetic changes are understood in terms of alterations of the MNP magnetic relaxation processes upon biomolecular recognition.[30,31] Biosensing methodologies are generally requested to avoid signal attenuation when operating in biological fluids.[32] This is the case for optical or colorimetric transduction, which regularly require sample purification procedures and/or to operate in limited spectral ranges[33,34] to not interfere with the displaying optical signal (i.e. emission, reflection, absorption). In contrast, magnetic methods have the potential to detect and/or quantify biomolecules directly in biological samples[35] without requiring further purification procedures. This simplification of the sample processing represents a remarkable advantage relying on the magnetic field penetration[36] in biological fluids, which due to their diamagnetic nature, weakly interact with magnetic fields. Indeed, many reported examples[21,22,25–29,37] of magnetic sensing methodologies found effective transduction when nanoparticles agglomerate driven by cross-linking between multiple bio-conjugated MNPs (b-MNPs) and target molecules. Such MNP and analyte agglomerates result in nano-clusters with hydrodynamic sizes (D_H) larger than individual MNPs.[22,25,26,28] Such MNP clustering leads to an increase of D_H[38] and intra-aggregate dipolar magnetic interactions,[39,40] which strongly influence the dynamical magnetization cycles. Alternatively, AC magnetometry (ACM) is a versatile and accurate technique employed for characterizing the influence of distinct intrinsic[39] and extrinsic[41–43] parameters on dynamical magnetization and magnetic losses of MNPs dispersed in liquid media, or inside cells.[43] Recent works[39] have shown the potential of this technique to directly probe MNP aggregation effects resulting from unspecific interactions between proteins and MNPs. Interestingly, ACM takes advantage of short acquisition times (few seconds) and reduced and sample volumes (tens of microlitres) to adequately probe biomolecular recognition dynamics while operating in a wide range of field conditions.[44] Moreover, ACM requires simple operational procedures (i.e. minimal sample preparation) for probing the presence of biomarkers in biological fluids.[45]

Here, we report on the proof of concept, and parametrization of a novel biosensing methodology based on variations of AC magnetic hysteresis areas measured in b-MNPs upon biomolecular recognition. We assessed the role of various parameters on modulating the changes of colloidal and AC magnetization properties of the resulting b-MNP assemblies. Namely, MNP and analyte concentrations, number of receptors per MNP, and analyte valency. Moreover, we evaluated how the nature of MNP magnetic relaxation mechanisms is extremely relevant to transduce biomolecular recognition between receptors and analytes. In addition, the biomolecular recognition triggers distinct assembly phenomena, resulting in nano-assemblies or nano-clusters depending on the analyte valency. In overall, the above-mentioned parameters strongly influence colloidal and AC magnetic properties, which modulates the analyte detection sensitivity allowing its customization. Part of our experimental findings were supported by numerical simulations to describe the AC magnetization cycles of individual b-MNP specifically interacting with multiple analytes and forming nano-assemblies.

Results and discussion

Experimental design of the proposed detection methodology. We employed magnetite and cobalt ferrite MNPs to bio-conjugate an engineered protein which acts as specific receptor for the analyte (see Fig. 1). The receptor is a designed peptide fused with a final MEEVF sequence to Glutathione S-transferase protein (GST) resulting in GST-MEEVF (see Material and Methods Section).[46] Table 1 lists the MNPs employed in this work for trapping mono- or divalent analytes. MNPs were conjugated to display the same average number of receptors onto MNP surface (around 20 receptors per b-MNP). According to transmission electron microscopy (TEM) and dynamic light scattering (DLS) data, b-MNPs are found to be individually dispersed in PB 0.1x buffer, where analytes preserve their structure and recognition capability. In order to study the effects of valency effects, we have chosen as analyte monomeric or dimeric Verde Fluorescent Protein (VFP) variants fused to the peptide-binding tetratricopeptide (TPR) domain (TPR2-MMY, which specifically interacts with MEEVF peptide).[47] Protein engineering allows the generation of mono-($VFP_{monomer}$-TPR2-MMY) or divalent (VFP_{dimer}-TPR2-MMY) TPR recognition molecules acting as analytes to specifically interact with the bio-conjugated GST-MEEVF receptor. While incubation of monomeric or dimeric VFP variants with b-MNPs during 1 hour at 25°C in 0.1x phosphate buffer (PB) in absence of external magnetic fields, biomolecular recognition results in different assembling (see Fig. 1). For monomer VFPs, nano-assemblies are formed between individual b-MNPs surrounded by multiple analytes specifically bound to the conjugated receptors. The latest leads to b-MNP surface modifications that strongly influence its translational diffusion. In case of dimer VFP, nano-clusters are formed after crosslinking between multiple b-MNPs and analytes, resulting in agglomerates whose D_H are larger than individual b-MNP. Such different b-MNP and analyte assemblies driven by the analyte variants raise up magnetic dipolar interactions, D_H and MNP diffusion, which strongly influence magnetic relaxation process.[39,48–50] Consequently, changes of AC magnetization cycles upon biomolecular recognition are expected to provide clear fingerprints of analyte detection in liquids (see Fig.1). Such transduction signal reflected in AC magnetization changes has been probed by ACM under alternating magnetic fields whose field frequency ranges from 10 till 300 kHz and intensities up to 24 kA/m. Recent works[51] have shown the relevance of field condition (i.e., field frequency and intensity value) to define a measurement time (τ_M) in order to probe the dynamic magnetization loops. Indeed, we take advantage of selecting field conditions to optimize the observation of alterations of magnetic relaxation times following b-MNP nano-assembly or nano-cluster formation. These alterations are reflected in AC magnetization loops, and therefore, the AC magnetic hysteresis area (A) is an adequate parameter to monitor the variations of dynamic magnetization loops upon biomolecular recognition (see Fig.1). Moreover, the normalization of the A value obtained in presence of a given analyte concentration upon the AC magnetic hysteresis area value in absence of analytes (A_0) offers an adequate parameter (A/A_0) to track the b-MNP transducing capacity at the

experimental conditions studied in this work. In this manner, we studied the influence of different parameters on the transducing sensitivity of the proposed methodology, as shown next.

Effect of MNP magnetic relaxation mechanisms on the b-MNPs transducing capacity for monovalent analyte detection. To unveil the role of the relaxation mechanisms on the b-MNP transducing capacity for detecting monovalent analyte, we employed bio-conjugated iron oxide (b-IONF) and cobalt ferrite (b-CoFeNFs) nanoflowers. We assigned the prevalence of Néel or Brownian relaxation mechanisms in IONFs and CoFeNFs, respectively, by looking at viscosity effects on AC magnetization cycles (see Fig. S1). Afterwards, we performed DLS, and ACM measurements to monitor the variations of D_H and A/A_0 in presence of monovalent analyte. As shown in Fig. 2a shows no significant variations of AC magnetization cycles were observed for b-IONF formulations on increasing monovalent analyte concentration up to 4 μM. Contrary, Fig. 2b depicted remarkable variations of AC magnetization cycles (shape and values) for b-CoFeNF formulation in the same analyte concentration range. Then, a progressive reduction of the normalized magnetic area (A/A_0) is observed up to 30 % at the highest analyte concentration (4 μM) for CoFeNFs. The origin of the distinct AC magnetization behaviour observed for IONFs and CoFeNFs after monovalent analyte recognition seems to be related to the distinct nature of their dominant magnetic relaxation process. On one hand, the prevalence of Brownian process for CoFeNFs allows to transduce the monovalent recognition down to 50 nM, while b-IONFs (for which Néel relaxation prevails) does not transduce even at the highest analyte concentration. On the other hand, different MNP size, shape and composition just define the extent of the variation of AC hysteresis loops after biomolecular recognition (see Fig. S2 for IONPs and CoFeNCs). It is worth noting the lowest analyte concentration (50 nM of monomer VFP variant) detected by this magnetic method corresponds to concentration values of clinical significance.[15,16]
Besides, Fig. 3c and d shows intensity weighted D_H values are maintained around 65 ± 0.5 nm with a polydispersity index (PDI) smaller than 0.2 on increasing monovalent analyte concentration for b-CoFeNFs and b-IONFs (see blue dots Fig. 3). Indeed, nano-assembling phenomena mediated by monovalent biomolecular recognition keeps individually dispersed b-MNPs after incubation. Only CoFeNFs show some agglomeration degree at analyte concentrations higher than 2 μM due to some unspecific interactions mediated by magnetic interactions due to their MNP blocked magnetic state[52] (see Fig. S3). Interestingly, translational diffusion coefficient varies depending on MNP surface (i.e. bare, bio-conjugated receptor or analyte bounded to receptor). As shown in Table S1, iron oxide (IONFs) and cobalt ferrite (CoFeNFs) nanoflowers both show a 12% progressive decrease of the translational diffusion coefficient values upon conjugation and after monovalent analyte recognition: from 10.3 ± 0.1 / 8.9 ± 0.5 x10^6 $nm^2/\mu s$ for bare CoFeNFs / IONFs down to 9.1 ± 0.2 / 7.7 ± 0.4 x10^6 $nm^2/\mu s$ for b-CoFeNFs / b-IONFs in presence of 2 μM monovalent analyte, respectively. However, the variation of diffusion coefficient is only reflected on the AC magnetization cycles measured for b-CoFeNFs due to the prevalence of Brownian relaxation on their magnetization relaxation dynamics. To confirm such assumption, we performed numerical simulation of AC hysteresis loops by using the stochastic Landau–Lifshitz–Gilbert equation and Brownian Dynamics algorithm. AC hysteresis loops of IONFs and CoFeNFs when distinct magnetic relaxation processes prevail were simulated. As shown in Fig.4, an outstanding agreement between experiments and numerical predictions is observed. Since b-MNPs remain individually dispersed in PB after biomolecular recognition, numerical simulations succeed to accurately describe the experimental observations just by considering the MNP dominant magnetic relaxation process, some experimental parameter values (see Tables S2 and S3) including MNPs diffusion coefficients. Our findings underline the relevance of the MNP magnetic relaxation mechanism for displaying the detection of monovalent analyte via AC magnetometry.

Effect of analyte multivalency on the transducing capacity of b-MNPs for analyte detection. To assess the role of the analyte multivalency on the transducing capacity of b-MNPs, we employed again b-IONFs and b-CoFeNFs formulations incubated at the standard conditions (1 $g_{Fe\ or\ Fe+Co}$/L of b-MNPs dispersed in 0.1x PB for 1 hour at 25°C) with the divalent analyte variant in a concentration range from 0 up to 4 μM. The biomolecular recognition of divalent analyte is expected to cross-link multiple b-MNPs and analytes resulting in nano-clusters with larger D_H than individual b-MNPs. In contrast to the monovalent case, variations of AC hysteresis loops are now observed for all b-MNPs after biomolecular recognition (see Fig. 2c and 2d). Indeed, Fig. 3 shows the raise of the intensity-weighted D_H values for b-CoFeNFs and b-IONFs on increasing divalent analyte concentration. The D_H increase is highly correlated to PDI, which reflects strong variability of nano-cluster formation (see Table S4), as recently predicted[38]. These clustering is commonly observed for all b-MNPs independently of their size, morphology, or coating (see Fig. S4 for b-IONP and b-FeCoNCs). However, the extent of changes in AC magnetization loops strongly depends on the b-MNP morphology and composition being more pronounced for b-CoFeNFs. Thus, divalent analyte contents down to 50 nM (i.e., 2 mg of protein per liter) are detectable at standard b-MNP formulation and incubations conditions (i.e. 20 recpetors per b-MNP, and 1 $g_{Fe\ or\ Fe+Co}$/L). At high analyte contents, A/A_0 values reduce up to 25 (40) % for b-IONFs, and up to 60 (80) % for b-CoFeNFs (see green dots in Fig. 3a and 3b) in presence of 2 (4) μM divalent analyte. Such strong differences of AC magnetic hysteresis area are understood in terms of D_H values and intra-cluster magnetic dipolar interactions.[39] Both parameters strongly influence Brownian and Néel magnetic relaxation processes, respectively. The linear correlation[53] between Brownian relaxation time and hydrodynamic volume renders CoFeNFs more sensitive to clustering effects than IONFs. On the other hand, the changes of Néel relaxation time are due to alteration of effective anisotropy via magnetic dipolar interactions between MNPs tightly depend on the number of MNPs and their spatial distribution into formed

nano-clusters.[49,50,54] Therefore, our observation underlines the relevance of nano-cluster formation to detect divalent analyte by AC magnetometry, independently of the magnetic relaxation process.

Effect of b-IONFs concentration on the transducing capacity for analyte detection. To assess the role of the MNP concentration on the transducing capacity of b-MNPs, we study the colloidal and dynamical magnetization of b-IONFs incubations at the standard conditions on increasing b-IONF concentration values above the AC magnetometer sensitivity(≈$0.3x10^{-3}Am^2$) from 0.5 up to 2 g_{Fe}/L at constant 0.75 μM divalent analyte concentration. Qualitatively, it is intuitive that MNP concentration would tightly influence the clustering formation mediated by cross-linking between multiple b-IONFs and divalent analytes. Crosslinking phenomena tightly depend on the number of receptors per b-MNP, molecular recognition affinity, and analyte and b-MNPs concentrations. Recent computational studies[38] correlate these key parameters with nano-clustering formation in terms of their size and their fractal MNP spatial distribution, at the limit of high receptor-analyte affinity. Fig. 5 depicts the D_H, *PDI* and normalized AC magnetic hysteresis area (A/A_0) extracted from AC hysteresis loops measured at 100 kHz and 24 kA/m on increasing iron concentration. At a first glance, we observed a strong reduction of D_H values from 110 down to 65 nm on increasing 4-fold MNP concentration, while *PDI* significantly decreases from 0.3 down to 0.14. In fact, AFM experiments reveal large variability in the spatial distribution of b-IONF into nano-clusters (see Fig. S5). Low MNP concentrations result in high D_H and *PDI* values at the studied analyte concentration (0.75 μM). Such behavior can be understood in terms of the increase of receptor availability to specifically interact with divalent analytes when increasing b-IONFs content. In other words, the probability of sharing divalent analytes among b-IONFs decreases on increasing the number of bio-conjugated nanoparticles. This is because the number of available receptors raises, and consequently, D_H and *PDI* diminish. As shown in Fig. S5, the absence of external magnetic field during incubation leads to a random spatial distribution of IONFs into nano-clusters, which is exclusively mediated by biomolecular recognition; i.e. the receptor – analyte affinity, the number of receptors, MNPs, and analytes present in 0.1x PB. As mentioned above, the evolution of D_H versus MNP concentration determines the dynamical magnetization response, and consequently, the transducing capacity of b-IONFs. In this regard, larger clusters favor magnetic dipolar interactions,[39,48,54,55] which strongly influence Néel relaxation. Fig. 5 depicts the MNP concentration dependence on the normalized A/A_0 hysteresis area, resulting in a progressive increase from 85% up to 97% when decreasing D_H. Our observation underlines the relevance of MNP concentration to modulate the nano-cluster formation, influencing D_H and PDI. Interestingly, the transducing capacity of b-MNPs benefits from low b-MNP concentrations (< 1 g_{Fe}/L) to detect divalent analytes.

Effect of number of receptors per MNP on the b-MNP transducing capacity for analyte detection. To assess the role of the number of receptors per b-MNP on the transducing capacity of b-MNPs, we probe the influence of the number of receptors (i.e., recognition ligands) per b-MNP on their transducing capacity by studying IONFs bio-conjugated with a distinct number of receptors bound onto the nanoparticle surface, ranging from 2 to 12 receptors per MNP. Next, b-IONFs were incubated at standard conditions with 1 μM divalent analyte. Fig. 6 shows the MNP-receptor ratio dependence of colloidal and AC magnetic properties (i.e. D_H, *PDI*, and normalized AC magnetic hysteresis area at 100 kHz and 24 kA/m). The results reflect the significant variation of D_H and *PDI* on increasing number of receptors per MNP. On one hand, larger D_H and *PDI* values are observed for the lowest MNP- receptor ratio (1:2), reaching values D_H = 214 nm and *PDI* = 0.55. On increasing ratios, D_H and *PDI* values progressively decrease down to 90 nm and 0.15, respectively. On the other hand, A/A_0 values progressively increase from 85% up to 100% when receptor-MNP ratios raise. Similarly to study b-MNP and analyte concentration effects, the AC magnetic hysteresis area behavior is tightly related to evolution of D_H values. Interestingly, large MNP-receptor ratios result in less efficient magnetic transduction. The reason is that the need of sharing divalent analyte between b-IONFs diminishes on increasing the number of receptors per particle. Consequently, D_H and *PDI* values shrink. Our experimental observations underline the role played by the number of receptors per MNP on clustering formation. Indeed, the MNP-receptor ratio effectively controls MNP clustering formation, and consequently, strongly influences the AC magnetization cycles. Interestingly, the transducing capacity of b-MNPs benefits from low number of receptors per nanoparticle at the studied analyte concentration range.

Effect of field conditions on the transducing capacity of b-MNPs for analyte detection. To assess the role of the field conditions in analyte detection, we prepared b-IONF and b-CoFeNFs incubations with 2 μM of mono or divalent analytes at the standard conditions described in previous sections. AC magnetization measurements were performed under alternating magnetic fields ranging from 10 up to 100 kHz and field intensities up to 24 kA/m. As shown in Fig. S6, the A and A_0 values tightly depend on field conditions, as well as the presence of analytes and MNP composition. At a first glance, A values observed for CoFeNFs are twice larger than those for b-IONFs. In addition, the frequency dependence of CoFeNF AC magnetic area shows decrease/raise-saturation-decrease of their hysteresis area values at 4/24 kA/m intensity values, respectively. Contrary, the AC magnetic area frequency behaviour remarkably differ for IONFs with field intensity. At 4 kA/m, a progressive decrease of AC magnetic area is observed on increasing field frequency value. At 24 kA/m, the AC magnetic area progressively increases (in Fig. S6). Such different behaviour for IONFs and CoFeNFs is understood by the appearance or not of minor cycles on increasing f (see Fig. S7). Except for b-IONFs incubated with monovalent analyte, biomolecular recognition phenomena in general reduce the AC magnetic area values with respect to the case in absence of analytes. To better quantify the variation of sensitivity at different field conditions, we monitor normalized magnetic area

(A/A_0). Fig. 7 depicts A/A_0 ranges from 100% down to 65% depending on MNP composition, analyte valency and field conditions. For b-CoFeNFs, we observed larger lowering of A/A_0 values for the divalent analyte than for the monovalent one, which maintains value around 70% almost independent on field conditions. For b-IONFs, A/A_0 values are maintained around zero for the mono valent case at all field conditions. However, for divalent case, IONFs showed a progressive lowering of A/A_0 values on increasing field frequency from 100 down to 90% at 24 kA/m. while A/A_0 values are maintained around 80% at 4 kA/m. The influence of field conditions on analyte detection sensitivity can be understood in terms on how AC hysteresis loops is tailored by external AC magnetic field. Recent magnetic studies[45] show the induced field transition between magnetically unblocked and blocked states. The field frequency (f) defines the measurement time ($\tau_m=1/2\pi f$) according to the magnetic field sweeping rate during magnetization measurements. Thermal fluctuations across the magnetic anisotropy barrier are behind the relaxation mechanism that determines the lag between external field and magnetic moment directions. Such time lag tailors the opening of AC magnetization cycles.[51] Moreover, field intensity (H_0) defines both the number of the MNP magnetic moments aligned with respect to the external field direction and the magnetic regime (linear or non-linear) in which magnetization dynamics occur In this manner, the field frequency and intensity probe MNP magnetic relaxation, defining the shape and values of AC magnetization cycles as shown in Fig. S7. Interestingly, our experimental evidences show how field conditions remarkably influence the transduction capacity of the studied MNP. Indeed, low field intensities benefit the observation of A/A_0 variations for more sensitive detection of divalent analytes (i.e. nano-clustering) in CoFeNFs (i.e. Brownian relaxation).

CONCLUSIONS

We report on the proof of concept, and parametrization of a novel and highly sensitive methodology for quick and direct detection of proteins dispersed in liquids. This methodology is based on the variation of AC magnetic hysteresis area obtained in b-MNPs upon specific interaction with the analyte variants. We have assessed the role of several parameters influencing the MNP transducing capacity. First, our observations underline the relevance of the dominant MNP magnetic relaxation nature for transducing the biomolecule interaction with b-MNPs under alternating magnetic fields. Brownian process benefits the transduction of specific interactions between b-MNPs and monovalent/divalent analytes with respect to Néel mechanism. Second, analyte valence defines assembling phenomenology leading to nano-assembling (i.e.surface modifications) or nano-cluster) (i.e. MNP and analyte cross-linked agglomeration), enabling analyte detection down to 0.05 and 4 μM. Numerical simulations support our hypothesis regarding surface modification effects on cobalt ferrite nanoparticles for monovalent detection, showing an outstanding agreement with experimental results. Third, the number of b-MNPs, and receptors per MNP influence the nano-cluster formation in similar manner to the analyte content. Interestingly, the transducing capacity of b-MNPs also benefits from a low MNP concentration and low number of receptors per MNP for analyte detection. Finally, the field conditions benefit the observation of changes of AC magnetization cycles after biomolecular recognition. The systematic description of the parameters tuning the sensitivity of the proposed methodology allows a precise sensing customization by tailoring the b-MNP design and AC magnetometry settings. In this manner, clinical biomarkers can be adequately detected by separately testing the relevance of each studied parameter in the sensitivity modulation. This approach will provide optimal detection settings for employing the proposed biosensing methodology as an alternative *in vitro* diagnosis test.

Experimental Section/Methods

Magnetic nanoparticles. Table 1 lists some structural and colloidal features of the four MNPs employed in this study: 1) commercial magnetite nanoflowers (IONFs), Synomag®-D (Product Code 104-56-701, Micromod Partikeltechnologie GmbH, Germany) coated with carboxylic poly(ethylene glycol) (PEG) and nanocrystal size 30±4 nm; 2) commercial maghemite nanoparticles (IONPs), supplied by Liquid Research Ltd., United Kingdom (Product HYPERMAG C) coated with carboxylic dimercaptosuccinic acid (DMSA) and nanocrystal size 16±4 nm; 3) commercial $Co_{0.3}Fe_{2.7}O_4$ nanoflowers (CoFeNFs), (Product Code 124-02-501; Micromod Partikeltechnologie GmbH, Germany) coated with carboxylic Dextran and nanocrystal size 32±5 nm; and 4) $Co_{0.7}Fe_{2.3}O_4$ nanocubes (CoFeNCs) coated with carboxylic with poly(maleic anhydride-alt-1-octadecene) (PMAO) and cube edge size of 20±3 nm were synthesized by thermal decomposition method following a receipt described elsewhere[56].

Nanocrystal size. The MNP size and shape were evaluated by TEM (see Fig. S8). JEOL 2100 microscope operating at 200 kV (point resolution 0.18 nm) at Centro Biología Molecular Severo Ochoa UAM-CSIC was employed. TEM images were examined through manual analysis of more than 150 particles randomly selected in different grid locations of TEM micrographs using Image-J software to obtain the mean size and size distribution listed in Table 1.

Quantification of iron content in the magnetic colloids. The Fe and Co concentration in the studied MNP magnetic suspensions was determined by inductively coupled plasma optical emission spectrometry in an ICP-OES (Perkin Elmer Optima 2100 DV) at Servicio de Análisis Químico, ICMM-CSIC (Madrid, Spain).

Receptors and analytes. Receptor (or recognition ligand) was a Glutathione S-transferase (GST) fused at the C-terminal end to an engineered peptide of 24 amino acids with a final MEEVF sequence (GST-MEEVF), for specific recognition of the MMY-TPR2 domain.[46] This domain has been fused to a monomeric or dimeric variant of VFP protein, resulting in mono ($VFP_{monomer}$-TPR2-MMY)[47] and divalent (VFP_{dimer}-TPR2-MMY) variants with one or two recognition sites, respectively. This strategy offers VFP with single or multivalency interacting with the same GST-MEEVF receptor.

MNP bio-conjugation. For the bio-conjugation of the employed MNP formulations, we take advantage of carboxylic groups present in all coatings listed in Table 1. To activate the present carboxylic groups in dextran, PEG and DMSA coating CoFeNFs, IONPs, and IONFs, respectively,

1 mL of MNPs at 2.5 g/L of magnetic element mass (Fe, or Fe+Co) were incubated 4 hours at 37 °C with 150 mmol of EDC per g of Fe/Fe+Co and 150 mmol of per g of NHS Fe/Fe+Co. Then, the MNP suspension was washed on centrifugal filters (amicon ultra) with a molecular weight cut off (MWCO) of 100 kD. Next, b-MNPs were redispersed in 10 mM sodium phosphate buffer pH 7.4 to a final volume of 1 mL, and the filtering cleaning was repeated three times. These MNPs with pre-activated carboxyl groups were incubated at 2.5 $g_{Fe/Fe+Co}$/L with 100 µl of GST-MEEVF fusion protein at 167 µM in PB buffer overnight at 37°C. Finally, b-MNPs were purified by gel filtration through a Sepharose 6 CLB column using PB. Diffusion measurements of b-MNPs and MNPs were performed to assess the presence of bio-conjugated GST-MEEVF onto MNP surface, resulting in translational diffusion changes. To activate the present carboxylic groups in CoFeNCs coated with PMAO,[57] 1 mL of CoFeNCs at 2.5 g_{Fe+Co}/L was incubated for 4 hours at 37°C with 150 mmol of EDC per g of Fe+Co, 75 mmol of NHS per g of Fe+Co and 10 µL of NaOH 1M. After that, the same GST-MEEVF bio-conjugation procedure was employed for IONFs and IONPs.

Preparation of b-MNPs with different number of receptors. First, nanoparticle tracking analyser (Nanosight NS300, Malvern, UK) was used to determine hydrodynamic size, translational diffusion coefficient, and the number of particles per mL (1,9x10^{12} IONF/mL) by diluting IONFs at 1g_{Fe}/L in a ratio 1:5000 in double distilled water (DDW). Secondly, in order to set bio-conjugation protocol to anchor single receptor per MNP, we took 500 µL of each MNP suspension at 2.5 g_{Fe}/L were preactivated accordingly with the previous protocol, with 150 µmol of EDC/g_{Fe} and 75 µmol of NHS/g_{Fe} (4 hours at 37°C). Later was washed on centrifugal filter (amicon ultra) and redispersed in PB buffer to a final volume of 1 mL. Carboxyl pre-activated MNPs were incubated with 5 µL of GST-MEEVF at 3 µM in a ratio 1 GST-MEEVF: 1 MNP, considering the number of particles measured by nanoparticle tracking analysis (NTA), overnight at 37°C. Afterwards, b-MNPs decorated with GST-MEEVF fusion protein was purified by filtration using a Sepharose 6 CLB column and concentrated to a final volume of 1 mL and MNP concentration of 1 g_{Fe}/L. Taking advantage of the analyte fluorescence, single molecule fluorescence spectroscopy was employed to quantify the number of receptors (*i.e.,* ligands) present onto b-MNP surface after incubation with monovalent analytes. We intentionally prepared and characterized by Single fluorescence spectroscopy (SFS) described in the next section, a b-MNP formulation with a MNP : receptor ratio 1 : 1. This allows us to set the MNP bioconjugation procedures at distinct MNP : receptor ratios 1: 2, 1: 4, 1: 8, and 1:12. For this, we added different volumes of GST-MEEVF at 3 µM (10 µL, 20 µL, 40 µL and 70 µL, respectively) to the preactivated MNPs.

Quantification of the number of recognition receptors. Single fluorescence spectroscopy was employed in order to accurately determine the average number of bio-conjugated recognition ligands per b-MNP and their particle distribution. In brief, fluorescent analytes attached to the immobilized MNPs were photobleached one at a time while monitoring the time evolution of analyte fluorescence intensity from analytes bound to receptors per MNP (Fig. S9). The spatially-localized intensity changes related to single fluorophore photobleaching reports on the number of fluorophores[58] at the particular location of b-MNPs on the coverslip. To prepare the sample for SFS, glass substrate coverslips (25x75mm Type #1.5 Glass) were first cleaned with Piranha solution and coated with a mixture of PEG5000 (Iris Biotech GmbH, Germany) and PEG10000-Biotin (Iris Biotech GmbH, Germany) mixture (1:10000) before adding streptavidin (Thermo Fisher Scientific) to fix the biotinylated b-MNP. Then, biotinylated b-MNPs were released to immobilize MNP onto coverslip. Single MNP photobleaching experiments were carried out in a custom-made total internal reflection fluorescence (TIRF) microscope.[59] An oil immersion objective UAPON 100xOTIRF (Olympus) was set on an IX73 Olympus microscope body. A 488 nm continuous wavelength laser (Sapphire, Coherent,USA) excites the analyte fluorescence at 520 nm. Excitation laser power was 10 mW (epifluorescence configuration) at the objective. The filter cube used was ZET405/488/561m-TRF (Chroma). Andor iXon 897 EMCCD camera was used for image acquisition with readout rate of 17 MHz on a 512 x 128 pixels image, electron multiplier set to 300, exposure was set to 20 ms (also determine considering the bleaching and blinking process), acquisition mode was frame transfer with Kinetics and vertical shift speed 3.3 µs. A continuous sequence of 1500 20ms frames was acquired for the analysis of photobleaching steps. Data analysis was performed in two steps. First, fluorescent complexes bound to the MNP were spatially localized using free software RapidStorm.[60] An fluorescence intensity trace was obtained for every MNP in the 1500-frames sequence. Second, the intensity traces for every MNP were subsequently analyzed with in-house developed software (MatLab). The employed software inputs are shown in Table S5. Only fluorescent complexes that showed a maximal to minimal intensity difference equal or larger than the fluorescence intensity of single $VFP_{monomer}$-TPR2-MMY analyte (previously calibrated) were considered. Accordingly, intensity changes were only counted as a bleaching step if the intensity change was equal or larger than single $VFP_{monomer}$-TPR2-MMY. To prevent misidentification due to blinking or noise events, it was required that intensity changes lasted for at least five consecutive frames (100 ms). These conditions were adapted to the nanoparticle fluorescent complexes from the literature.[61,62] After filtering fluorescent complexes and photobleaching steps described above, the photobleaching steps were counted on each fluorescent b-MNP to perform statistical analysis to determine the number of receptors per MNP (see Fig. S10). For all experiments a minimum of 5000 particles were analyzed.

Analyte and b-MNP incubation conditions. 50 µL of the MNP formulations at given MNP content ranging from 0.5 up to 2 $g_{Fe/Fe+Co}$/L were incubated in PB 0.1x buffer for 1 hour at 25°C with different analyte variants at distinct analyte concentrations from 0 (control) up to 4 µM . All incubations were performed in absence of external magnetic fields.

Hydrodynamic size measurements. DLS measurements were performed to determine the intensity, number and volume weighted D_H of the b-MNPs at different experimental conditions. For that purpose, we employed a Zetasizer Nano ZS90 (Malvern Instruments, United Kingdom) equipped with a 4 mW He−Ne laser operating at 633 nm as energy source, with an angle of 173˚ between the incident beam and the avalanche photodiode detector. DDW and PB were used as dispersion media for measuring the colloidal properties of MNPs before bio-conjugation. Otherwise, the colloidal properties of b-MNPs at different MNP and analyte concentrations were studied in PB 0.1x buffer. b-MNPs were diluted to a final MNP concentration of 0.05 $g_{Fe/Fe+Co}$/L in 1 mL volume

deposited into a commercial cuvette prior automatic scan measurements (three scans per measurement).

Diffusion coefficient measurements. Table S1 lists the translational diffusion coefficient of IONFs and CoFeNFs in PB 0.1x buffer were carried out by NTA(Nanosight NS300, Malvern Instruments, United Kingdom). Bare and bio-conjugated MNP suspensions at an initial concentration of 1 $g_{Fe/Fe+Co}$/L were diluted 1:5000 in PB 0.1x buffer and injected into the instrument chamber using a 1 mL syringe. Camera settings were adjusted to focus the objective and track the individual Brownian motion of 20-80 MNP in the camera cell (see Fig. S11). Video data were recorded for 30 seconds and repeated 5 times per sample.

Magnetic characterization. Magnetization cycles under quasi-static conditions of MNPs dispersed in DDW were performed at different temperatures (4 and 300 K) in Quantum Design SQUID magnetometer model MPMS-XL at Técnicas Físicas, Universidad Complutense de Madrid (Madrid, Spain). The measured samples were 100 µL MNP dispersion volumes at concentration of 1$g_{Fe/Fe+Co}$/L. The magnetization values were normalized to the magnetic element mass (Fe or Fe+Co) of each measured suspension (see Fig.S12 at Supporting Information). AC magnetometry measurements of the magnetic colloids with a magnetic element mass ranging from 20 up to 80 µg were performed by commercial inductive magnetometers (SENS and ADVANCE AC Hyster™ Series , Nanotech Solutions, Spain). AC Hyster Series measure magnetization cycles from MNPs dispersed in liquid media at room temperature under alternating magnetic fields whose frequency ranges from 10 up to 300 kHz and intensities up to 24 kA/m. Each AC magnetization measurement consists of three repetitions to obtain an average of the magnetization cycles and the related magnetic parameters (H_C, M_R, AC magnetic hysteresis area). Such dynamical magnetization measurements take less than 60 seconds. Magnetization units were normalized by the magnetic element mass (*i.e.,* iron or iron plus cobalt magnetic elements) and expressed in Am^2/kg.

Computational simulations. Numerical simulations of MNP's AC magnetization cycles were performed to understand AC magnetic hysteresis area behaviour observed for CoFeNFs and IONFs nano-assemblies by using the multiphysics UAMMD software.[63,64] The latest is an open source framework running in graphical processor units equipped with immersed boundary[65] and Brownian based[66] colloidal hydrodynamics, recently generalised to include magnetic interactions between MNPs. Notably, the magnetic-UAMMD uses the single domain approach to solve the internal dynamics of the magnetization involving Néel relaxation and their coupling with MNP Brownian motion. The internal dynamics of the MNP magnetization $\vec{m}$(t) is solved by integrating the Landau-Lifshitz-Gilbert equation, following the scheme used in Vinamax code[67] :

$$\frac{d\vec{m}}{dt} = \frac{-\gamma_0}{1+\alpha^2}\left(\vec{m}\times\vec{B}_{eff} + \alpha\,\vec{m}\times\vec{m}\times\vec{B}_{eff}\right)$$

where γ_0 =1.7595 × 10^{11} rad/Ts denotes the gyromagnetic ratio, α the Gilbert damping constant, $\vec{m}$(t) a unitary vector parallel to the direction of the MNP magnetic moment; $\vec{B}_{eff} = \vec{B}_{an} + \vec{B}_{th} + \mu_0\vec{H}_{AC}$ is the effective magnetic field acting on each MNP composed by anisotropy field ($\vec{B}_{anis}$), the thermal field ($\vec{B}_{therm}$), and external magnetic field ($\vec{H}_{AC}$). Note that the dilute MNP concentration employed in the experiments allows to neglect magnetic interacting phenomena between MNPs. The anisotropy field was calculated as,

$$\vec{B}_{anis} = \frac{2K}{M_{sat}}\cdot(\vec{m}\cdot\hat{u})\cdot\hat{u}$$

where *K* is the MNP anisotropy constant, M_{sat} is the saturation magnetization value of the MNP ensemble, and $\hat{u}$ the unit vector denoting the easy axis direction of MNP. The thermal field described the effect of thermal fluctuations arising from MNP magnetic monodomain and satisfies the fluctuation-dissipation relation derived by Brown [68] :

$$\vec{B}_{therm} = \sqrt{\frac{2k_BT\,\alpha}{\gamma_0 M_{sat}V_c dt}}\cdot\vec{W}$$

where k_B denotes the Boltzman constant, T the temperature of the system, V_c the volume of the magnetic core of the particle, dt the time step, and $\vec{W}$ is a random force delta-correlated $\langle W_i(t)W_j(0)\rangle = \delta(t)\delta_{ij}$ and zero average. The external magnetic field ($\vec{H}_{AC}$) defined by a time dependent sinusoidal wave with field amplitude (i.e. intensity) H_0 and frequency f:

$$\vec{H}_{AC} = \vec{H}_0\cdot\sin(2\pi f\cdot t)$$

Brownian dynamics of each MNP orientation is solved by using the corresponding overdamped of each particle is computed in every time step as :

$$d\vec{\phi} = -M_r\cdot\overrightarrow{\tau_{AC}}\cdot dt + \sqrt{2k_BTM_r}\cdot\overrightarrow{dW}$$

where $\overrightarrow{dW}$ is a vector of independent Wiener increments (three random components with zero mean, and unit variance, i.e. $\langle dW_i^2\rangle$ = dt). We use $M_r = \frac{1}{\pi\eta D_H^3}$ for the rotational mobility of a spherical colloid, while $\overrightarrow{\tau_{AC}}$ is the torque exerted by the field on the particles,

$$\overrightarrow{\tau_{AC}} = \mu_0\cdot\vec{M}\times\overrightarrow{H_{AC}}$$

where $\vec{M} = M_{sat}\cdot V_C\cdot\vec{m}$ is the MNP magnetic moment. Values of M_{sat} and *K* were obtained from quasi-static magnetization measurements at 4 and 300 K (see Table S2). V_C was obtained from MNP TEM images. Simulations considered the MNP size Gaussian distribution, mean size and standard deviation observed by TEM images (see Table S3). Depending on the predominant relaxation mechanism of the particles (i.e. Brown or Neel) the procedure employed to simulate the cycles was slightly different. When the predominant mechanism is Néel, AC magnetization cycles are not sensitive to changes in the hydrodynamic size. Hence, it was enough

to perform the simulations using the same hydrodynamic size for all the particles. The value of the hydrodynamic size was obtained from the experimental measurements of the translational diffusion coefficient of the particles (Table S1). Contrary, when the predominant relaxation mechanism is Brown, AC magnetization cycles are extremely sensitives to changes the distribution of hydrodynamics sizes. For that reason, it was necessary to consider not only the mean hydrodynamic size of the particles but also their distribution. In this simulations we have considered a log-normal distribution of hydrodynamic sizes [69–71]:

$$p(D_h) = \frac{1}{D_h \sigma \sqrt{2\pi}} \exp\left(-\frac{(\ln(D_h) - \mu)^2}{2\sigma^2}\right)$$

where μ and σ are related with the mean hydrodynamic size ($\langle D_h \rangle$) and the standard deviation of the distribution (STD) through:

$$\mu = \ln\left(\frac{\langle D_h \rangle^2}{\sqrt{\langle D_h \rangle^2 + STD^2}}\right)$$

$$\sigma^2 = \ln\left(1 + \frac{STD^2}{\langle D_h \rangle^2}\right)$$

The values of $\langle D_h \rangle$ and STD were determined by performing unbiased random samplings in which both magnitudes (employed as input parameters for the simulations) were varied until the experimental magnetization cycles were accurately fitted. In order to speed up these samplings, we benefited from the large anisotropy energy in comparison to thermal energy; i.e $KV \gg k_B T$. In this way, the rigid dipole approximation[72–74] (i.e. $\vec{M}$ aligned to MNP magnetization easy axis) is assumed. Hence, we avoid costly calculation of the internal dynamics of the magnetization, which otherwise require quite small-time steps, in comparison to those employed for solving MNP Brownian motion. Once the optimal MNP size-distribution was found, we removed the adiabatic approximation for the magnetization vector and reproduced the experimental cycles solving the Landau-Lifshitz-Gilbert equation, to verify the validity of this approach.

Author contributions

FJT and ALC designed the research. NC and TP synthesized and characterized CoFeNCs. ESD, AA, DC, and EJAI performed the bio-conjugations, DLS, NTA and AC magnetization experiments. PPA and RDB performed simulations. CCV and JRI performed single molecule fluorescent experiments. ESD, AA, DC, ALC, and FJT analyzed and discussed the results. ESD and FJT wrote the first draft and the rest of authors contributed to tail the submitted and revised manuscript.

Conflicts of interest

There are no conflicts to declare.

Acknowledgements

This work has been partially funded by the Spanish State Research Agency (PCI2019-103600, CEX2020-001039-S, MDM-2017-0720, PID2019-111649RB-I00, PID2020-117080RB-C51, PID2020-117080RB-C53, PID2019-111649RB-I00, PDC2021-120957-I00, PDC2022-133345-I00, and Hipernano, RED2018-102626-T, PTA2018-015076) and Comunidad de Ma-drid (PEJ-2017-AI/BMD-7517, PEJ-2020-AI/IND-19394, NANOMAGCOST S2018/NMT-4321). COST Actions CA17115 (MyWave), and CA17140 (Nano2Clinic) are also acknowledged. This work was partially supported by the European Union's Horizon 2020 research and innovation programme under the Marie Sklodowska-Curie HeatnMof grant (GA No. 860942).

References

1 F. Vahedifard and K. Chakravarthy, *Emergent Mater.*, 2021, **4**, 75–99.

2 S. B. Nimse, M. D. Sonawane, K.-S. Song and T. Kim, *The Analyst*, 2016, **141**, 740–755.

3 C. L. Sawyers, *Nature*, 2008, **452**, 548–552.

4 N. Shaabani, S. R. Meira, M. Marcet-Palacios and M. Kulka, *ACS Pharmacol. Transl. Sci.*, 2023, **6**, 387–398.

5 X. Wang, R. Xu, X. Sun, Y. Wang, X. Ren, B. Du, D. Wu and Q. Wei, *Biosens. Bioelectron.*, 2017, **96**, 239–245.

6 X. Yu, B. Munge, V. Patel, G. Jensen, A. Bhirde, J. D. Gong, S. N. Kim, J. Gillespie, J. S. Gutkind, F. Papadimitrakopoulos and J. F. Rusling, *J. Am. Chem. Soc.*, 2006, **128**, 11199–11205.

7 V. Palomo, S. A. Díaz, M. H. Stewart, K. Susumu, I. L. Medintz and P. E. Dawson, *ACS Nano*, 2016, **10**, 6090–6099.

8 D. Mendez-Gonzalez, M. Laurenti, A. Latorre, A. Somoza, A. Vazquez, A. I. Negredo, E. López-Cabarcos, O. G. Calderón, S. Melle and J. Rubio-Retama, *ACS Appl. Mater. Interfaces*, 2017, **9**, 12272–12281.

9 F. Ghasemi, M. R. Hormozi-Nezhad and M. Mahmoudi, *Nanoscale*, 2018, **10**, 6361–6368.

10 P. Moitra, M. Alafeef, K. Dighe, M. B. Frieman and D. Pan, *ACS Nano*, 2020, **14**, 7617–7627.

11 B. D. Malhotra and Md. A. Ali, in *Nanomaterials for Biosensors*, eds. B. D. Malhotra and Md. A. Ali, William Andrew Publishing, 2018, pp. 1–74.

12 W. Zhou, K. Hu, S. Kwee, L. Tang, Z. Wang, J. Xia and X. Li, *Anal. Chem.*, 2020, **92**, 2739–2747.

13 T. A. P. Rocha-Santos, *TrAC Trends Anal. Chem.*, 2014, **62**, 28–36.

14 L. Gloag, M. Mehdipour, D. Chen, R. D. Tilley and J. J. Gooding, *Adv. Mater.*, 2019, **31**, 1904385.

15 D. Sim, M. C. Brothers, J. M. Slocik, A. E. Islam, B. Maruyama, C. C. Grigsby, R. R. Naik and S. S. Kim, *Adv. Sci.*, 2022, **9**, 2104426.

16 M. Ouyang, D. Tu, L. Tong, M. Sarwar, A. Bhimaraj, C. Li, G. L. Coté and D. Di Carlo, *Biosens. Bioelectron.*, 2021, **171**, 112621.

17 F. Gambinossi, S. E. Mylon and J. K. Ferri, *Reinhard Mill. Honor. Issue*, 2015, **222**, 332–349.

18 G. Fu, S. T. Sanjay, W. Zhou, R. A. Brekken, R. A. Kirken and X. Li, *Anal. Chem.*, 2018, **90**, 5930–5937.

19 A. Latorre, C. Posch, Y. Garcimartín, S. Ortiz-Urda and Á. Somoza, *Chem. Commun.*, 2014, **50**, 3018–3020.

20 M. Donolato, P. Antunes, R. S. Bejhed, T. Zardán Gómez de la Torre, F. W. Østerberg, M. Strömberg, M. Nilsson, M. Strømme, P. Svedlindh, M. F. Hansen and P. Vavassori, *Anal. Chem.*, 2015, **87**, 1622–1629.

21 A. Moyano, M. Salvador, J. C. Martínez-García, V. Socoliuc, L. Vékás, D. Peddis, M. A. Alvarez, M. Fernández, M. Rivas and M. C. Blanco-López, *Anal. Bioanal. Chem.*, 2019, **411**, 6615–6624.

22 J. M. Perez, F. J. Simeone, Y. Saeki, L. Josephson and R. Weissleder, *J. Am. Chem. Soc.*, 2003, **125**, 10192–10193.

23 Z. Ma, J. Mohapatra, K. Wei, J. P. Liu and S. Sun, *Chem. Rev.*, , DOI:10.1021/acs.chemrev.1c00860.

24 G. Mistlberger, K. Koren, E. Scheucher, D. Aigner, S. M. Borisov, A. Zankel, P. Pölt and I. Klimant, *Adv. Funct. Mater.*, 2010, **20**, 1842–1851.

25 A. Fornara, P. Johansson, K. Petersson, S. Gustafsson, J. Qin, E. Olsson, D. Ilver, A. Krozer, M. Muhammed and C. Johansson, *Nano Lett.*, 2008, **8**, 3423–3428.

26 S. Gandhi, H. Arami and K. M. Krishnan, *Nano Lett.*, 2016, **16**, 3668–3674.

27 S. Schrittwieser, F. Ludwig, J. Dieckhoff, K. Soulantica, G. Viau, L.-M. Lacroix, S. M. Lentijo, R. Boubekri, J. Maynadié, A. Huetten, H. Brueckl and J. Schotter, *ACS Nano*, 2012, **6**, 791–801.

28 J. Zhong, E. L. Rösch, T. Viereck, M. Schilling and F. Ludwig, *ACS Sens.*, 2021, **6**, 976–984.

29 T. Mizoguchi, A. Kandori, R. Kawabata, K. Ogata, T. Hato, A. Tsukamoto, S. Adachi, K. Tanabe, S. Tanaka, K. Tsukada, and K. Enpuku, *IEEE Trans. Appl. Supercond.*, 2016, **26**, 1–4.

30 A. R. Chalifour, J. C. Davidson, N. R. Anderson, T. M. Crawford and K. L. Livesey, *Phys. Rev. B*, 2021, **104**, 094433.

31 C. Min, H. Shao, M. Liong, T.-J. Yoon, R. Weissleder and H. Lee, *ACS Nano*, 2012, **6**, 6821–6828.

32 M. Varshney and K. Mallikarjunan, 2009, **16**, 18–21.

33 E. Hemmer, A. Benayas, F. Légaré and F. Vetrone, *Nanoscale Horiz.*, 2016, **1**, 168–184.

34 F.-X. Schmid, in *Encyclopedia of Life Sciences*, 2001.

35 S. Hildebrand, N. Löwa, H. Paysen, R. M. Fratila, L. Reverte-Salisa, T. Trakoolwilaiwan, Z. Niu, G. Kasparis, S. F. Preuss, O. Kosch, J. M. de la Fuente, N. T. K. Thanh, F. Wiekhorst and A. Pfeifer, *ACS Nano*, 2021, **15**, 434–446.

36 M. Meister, *eLife*, 2016, **5**, e17210.

37 K. Wu, D. Tonini, S. Liang, R. Saha, V. K. Chugh and J.-P. Wang, *ACS Appl. Mater. Interfaces*, 2022, **14**, 9945–9969.

38 P. Palacios-Alonso, E. Sanz-de Diego, Raúl P. Peláez, A. L. Cortajarena, F.J. Teran, and Rafael Delgado-Buscalioni, .

39 J. G. Ovejero, D. Cabrera, J. Carrey, T. Valdivielso, G. Salas and F. J. Teran, *Phys. Chem. Chem. Phys.*, 2016, **18**, 10954–10963.

40 L. C. Branquinho, M. S. Carrião, A. S. Costa, N. Zufelato, M. H. Sousa, R. Miotto, R. Ivkov and A. F. Bakuzis, *Sci. Rep.*, 2013, **3**, 2887.

41 D. Cabrera, A. Lak, T. Yoshida, M. E. Materia, D. Ortega, F. Ludwig, P. Guardia, A. Sathya, T. Pellegrino and F. J. Teran, *Nanoscale*, 2017, **9**, 5094–5101.

42 N. Telling, in *Nanomaterials for Magnetic and Optical Hyperthermia Applications*, Elsevier, 2019, pp. 173–197.

43 D. Cabrera, A. Coene, J. Leliaert, E. J. Artés-Ibáñez, L. Dupré, N. D. Telling and F. J. Teran, *ACS Nano*, 2018, **12**, 2741–2752.

44 S. Ota, R. Kitaguchi, R. Takeda, T. Yamada and Y. Takemura, *Nanomaterials*, , DOI:10.3390/nano6090170.

39 Aires, A., Cabrera, D., Artés, E., Cortajarena, A. & Teran, F. METHOD FOR DETECTION OF AN ANALYTE. (2019).

46 M. E. Jackrel, R. Valverde and L. Regan, *Protein Sci.*, 2009, NA-NA.

47 R. P. Ilagan, E. Rhoades, D. F. Gruber, H.-T. Kao, V. A. Pieribone and L. Regan, *FEBS J.*, 2010, **277**, 1967–1978.

48 D. Serantes, K. Simeonidis, M. Angelakeris, O. Chubykalo-Fesenko, M. Marciello, M. del P. Morales, D. Baldomir and C. Martinez-Boubeta, *J. Phys. Chem. C*, 2014, **118**, 5927–5934.

49 M. V. Zyuzin, M. Cassani, M. J. Barthel, H. Gavilan, N. Silvestri, A. Escudero, A. Scarpellini, F. Lucchesi, F. J. Teran, W. J. Parak and T. Pellegrino, *ACS Appl. Mater. Interfaces*, 2019, **11**, 41957–41971.

50 E. Ximendes, R. Marin, Y. Shen, D. Ruiz, D. Gómez-Cerezo, P. Rodríguez-Sevilla, J. Lifante, P. X. Viveros-Méndez, F. Gámez, D. García-Soriano, G. Salas, C. Zalbidea, A. Espinosa, A. Benayas, N. García-Carrillo, L. Cussó, M. Desco, F. J. Teran, B. H. Juárez and D. Jaque, *Adv. Mater.*, 2021, **33**, 2100077.

51 D. Cabrera, T. Yoshida, T. Rincón-Domínguez, J. L. F. Cuñado, G. Salas, A. Bollero, M. del P. Morales, J. Camarero and F. J. Teran, *Nanoscale*, , DOI:10.1039/D2NR00808D.

52 F. L. Durhuus, L. H. Wandall, M. H. Boisen, M. Kure, M. Beleggia and C. Frandsen, *Nanoscale*, 2021, **13**, 1970–1981.

53 J. Dieckhoff, D. Eberbeck, M. Schilling and F. Ludwig, *J. Appl. Phys.*, 2016, **119**, 043903.

54 D. Niculaes, A. Lak, G. C. Anyfantis, S. Marras, O. Laslett, S. K. Avugadda, M. Cassani, D. Serantes, O. Hovorka, R. Chantrell and T. Pellegrino, *ACS Nano*, 2017, **11**, 12121–12133.

55 C. Martinez-Boubeta, K. Simeonidis, D. Serantes, I. Conde-Leborán, I. Kazakis, G. Stefanou, L. Peña, R. Galceran, L. Balcells, C. Monty, D. Baldomir, M. Mitrakas and M. Angelakeris, *Adv. Funct. Mater.*, 2012, **22**, 3737–3744.

56 A. Sathya, P. Guardia, R. Brescia, N. Silvestri, G. Pugliese, S. Nitti, L. Manna and T. Pellegrino, *Chem. Mater.*, 2016, **28**, 1769–1780.

57 R. Di Corato, A. Quarta, P. Piacenza, A. Ragusa, A. Figuerola, R. Buonsanti, R. Cingolani, L. Manna and T. Pellegrino, *J. Mater. Chem.*, 2008, **18**, 1991.

58 P. Tinnefeld, C. Eggeling and S. W. Hell, Eds., *Far-Field Optical Nanoscopy*, Springer Berlin Heidelberg, Berlin, Heidelberg, 2015, vol. 14.

59 M. L. MARTIN-FERNANDEZ, C. J. TYNAN and S. E. D.

WEBB, *J. Microsc.*, 2013, **252**, 16–22.

60 S. Wolter, A. Löschberger, T. Holm, S. Aufmkolk, M.-C. Dabauvalle, S. van de Linde and M. Sauer, *Nat. Methods*, 2012, **9**, 1040–1041.

61 S. E. D. Webb, M. Hirsch, S. R. Needham, B. C. Coles, K. M. Scherer, S. K. Roberts, L. C. Zanetti-Domingues, C. J. Tynan, M. L. Martin-Fernandez and D. J. Rolfe, *Super-Resolut. Light Microsc.*, 2015, **88**, 76–80.

62 S. R. Needham, M. Hirsch, D. J. Rolfe, D. T. Clarke, L. C. Zanetti-Domingues, R. Wareham and M. L. Martin-Fernandez, *PLOS ONE*, 2013, **8**, 13.

63 Pérez Peláez, Raúl, Universally Adaptable Multiscale Molecular Dynamics https://github.com/RaulPPelaez/UAMMD.

64 Pérez Peláez, Raúl, *Complex fluids in the Gpu era. Algorithms and simulations*, UAM. Departamento de Física Teórica de la Materia Condensada.

65 A. Vázquez-Quesada, F. Balboa Usabiaga and R. Delgado-Buscalioni, *J. Chem. Phys.*, 2014, **141**, 204102.

66 S. Delong, F. B. Usabiaga, R. Delgado-Buscalioni, B. E. Griffith and A. Donev, *J. Chem. Phys.*, 2014, **140**, 134110.

67 J. Leliaert, A. Vansteenkiste, A. Coene, L. Dupré and B. Van Waeyenberge, *Med. Biol. Eng. Comput.*, 2015, **53**, 309–317.

68 W. F. Brown, *Phys. Rev.*, 1963, **130**, 1677–1686.

69 S. G. Sherman and N. M. Wereley, *IEEE Trans. Magn.*, 2013, **49**, 3430–3433.

70 W. Liu, M. Zhou and L. Kong, *Meas. Sci. Technol.*, 2009, **20**, 125802.

71 R. M. Ferguson, K. R. Minard, A. P. Khandhar and K. M. Krishnan, *Med. Phys.*, 2011, **38**, 1619–1626.

72 S. W. Davis, W. McCausland, H. C. McGahagan, C. T. Tanaka and M. Widom, *Phys. Rev. E*, 1999, **59**, 2424–2428.

73 J. P. Huang, Z. W. Wang and C. Holm, *Phys Rev E*, 2005, **71**, 061203.

74 Z. Wang, C. Holm and H. W. Müller, *Phys. Rev. E*, 2002, **66**, 021405.

FIGURES AND TABLES

Table 1. Summary of structural, and colloidal parameters of the studied MNPs when dispersed in DDW.

MNP	Composition	Shape	TEM size (nm)	Coating	D_H intensity (nm)	D_H number (nm)	D_H volume (nm)	PDI	ξ potential (mV)
IONFs	Fe_3O_4	Nanoflower	30 ± 4	Dextran-PEG	65 ± 0.5	40 ± 2	53 ± 1.5	0.12	- 5
IONPs	Fe_3O_4	Polyhedron	16 ± 4	DMSA	93 ± 0.4	21 ± 3.1	118 ±0.4	0.19	- 38
CoFeNFs	$Co_{0.3}Fe_{2.7}O_4$	Nanoflower	32 ± 5	Dextran	52 ± 0.6	41 ± 0.6	48 ± 0.6	0.08	- 8
CoFeNCs	$Co_{0.7}Fe_{2.3}O_4$	Cubic	20 ± 3	PMAO	69 ± 26	37 ± 11	49 ± 0.2	0.12	- 45

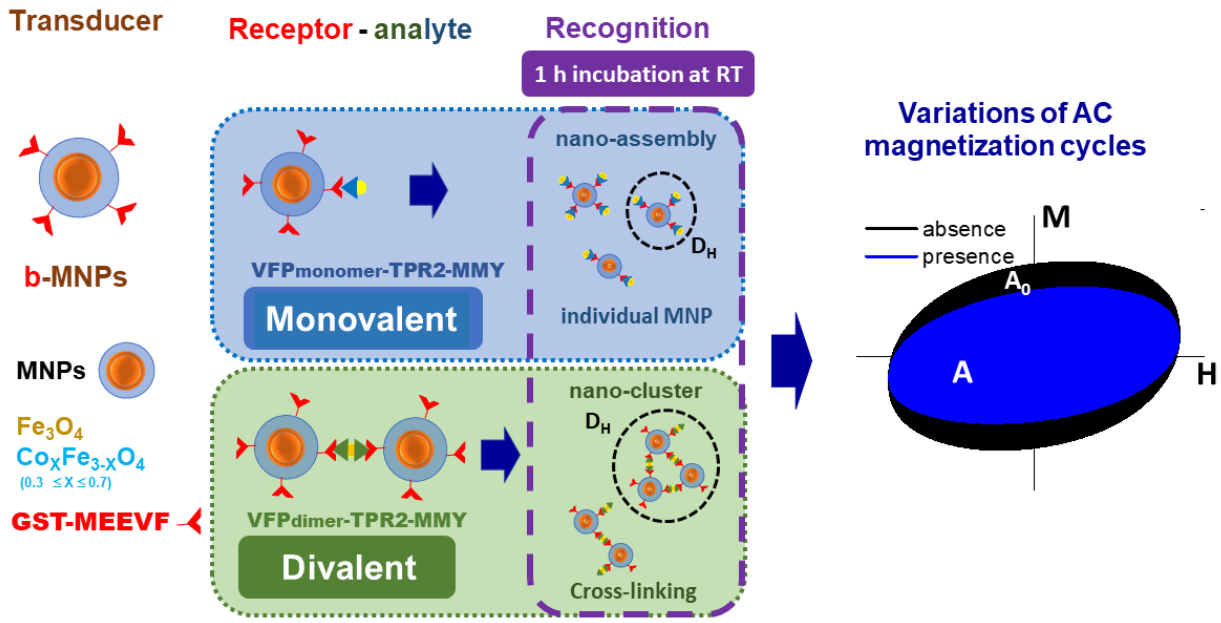

Fig.1. Schematic representation of the detection methodology based on the variations of the AC magnetic hysteresis area in absence (A_0), and presence (A) of VFP analyte variants. Individual (nano-assembly) or cross-linked (nano-cluster) assemblies are formed after biomolecular recognition between (GST-MEEVF) conjugated receptors, and $VFP_{monomer}$- or VFP_{dimer}-TPR2-MMY variants. Incubation conditions: at given b-MNP and analyte concentrations dispersed in 0.1x PB for 1 hour at 25°C in absence of external magnetic field.

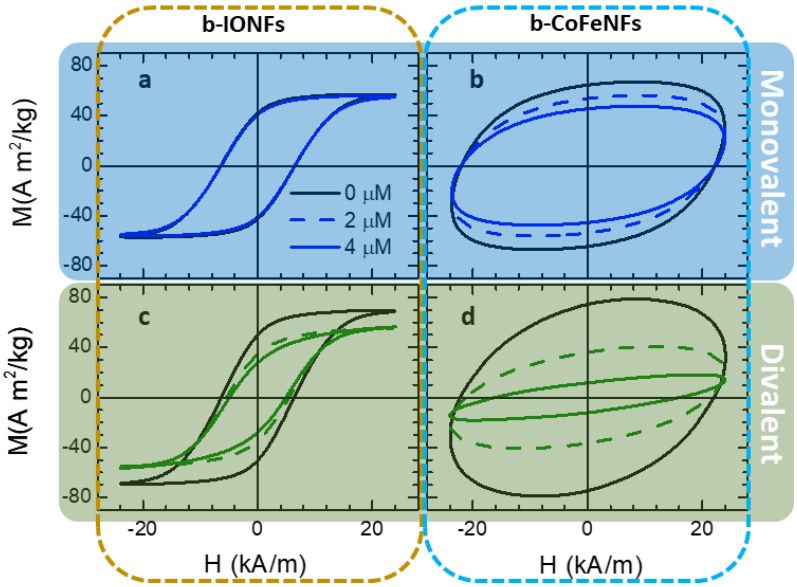

Fig. 2. AC hysteresis loops of the b-IONFs (right) and b-CoFeNFs (left) after incubation with mono- and divalent analytes at different concentrations. AC magnetization measurements were performed under AC field conditions: (a,c) 100 kHz and 24 kA/m; (b,d) 30 kHz and 24 kA/m. Incubation conditions: b-MNPs ($1g_{Fe\ or\ Fe+Co}$/L) dispersed in 0.1x PB for 1h at 25°C.

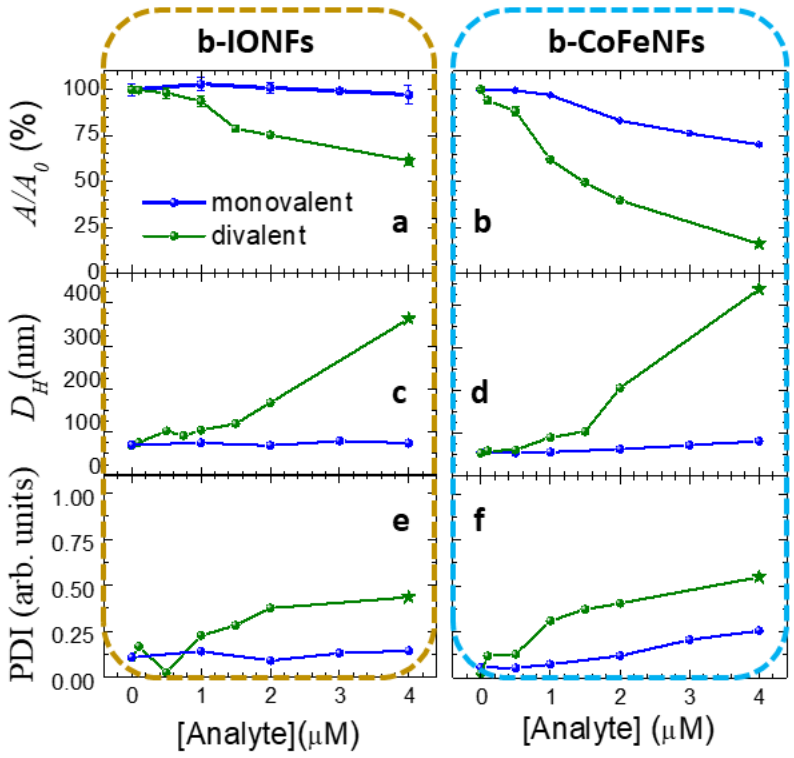

Fig. 3. Analyte concentration dependence of normalised AC magnetic area (A/A_0) extracted from AC hysteresis loops of a) b-IONFs suspensions at 100 kHz and 24 kA/m; b) b-CoFeNFs suspensions at 30 kHz and 24 kA/m. Analyte concentration dependence of D_H values obtained from: c) b-IONFs suspensions; d) b-CoFeNFs suspensions. Analyte concentration dependence of PDI values obtained for: e) b-IONFs suspensions; f) b-CoFeNFs suspensions. Incubation conditions: b-MNPs ($1g_{Fe\ or\ Fe+Co}/L$) dispersed in 0.1x PB for 1h at 25°C on increasing analyte mono (blue colour) or divalent (green colour) concentrations. Star symbols indicate the sedimentation of magnetic suspensions prior magnetization measurements.

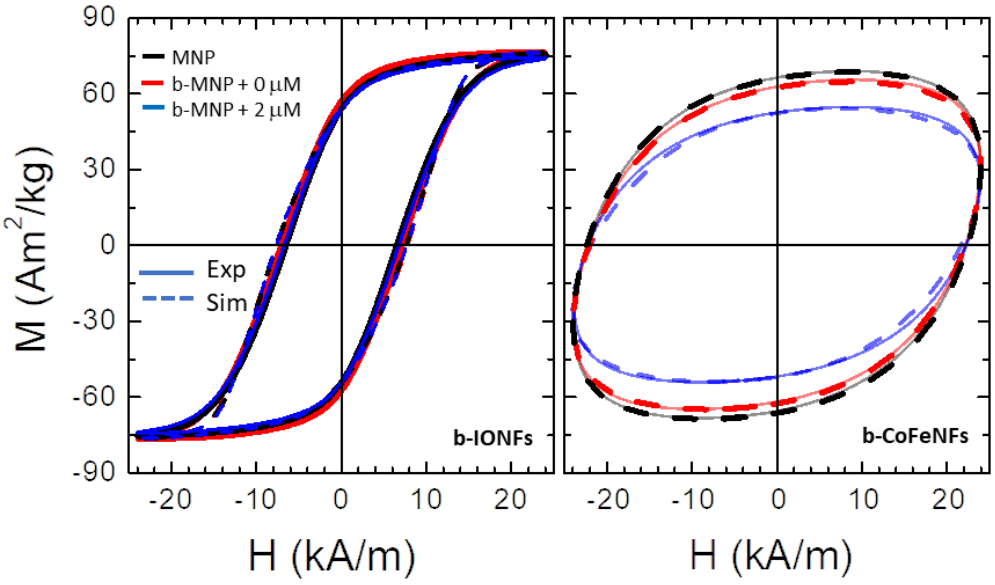

Fig. 4. Experimental (solid lines) and simulated (dashed lines) AC hysteresis loops for: Left) IONFs (black line), b-IONFs in absence (red line) and in presence (blue line) of monovalent analyte at 100 kHz and 24 kA/m; Right) CoFeNFs (red line), b-CoFeNFs in absence (black line) and in presence (blue line) of monovalent analyte at 40 kHz and 24 kA/m. Incubation conditions: b-MNPs (1$g_{Fe\ or\ Fe+Co}$/L) and 2 µM monovalent analytes dispersed in 0.1x PB for 1 h at 25°C.

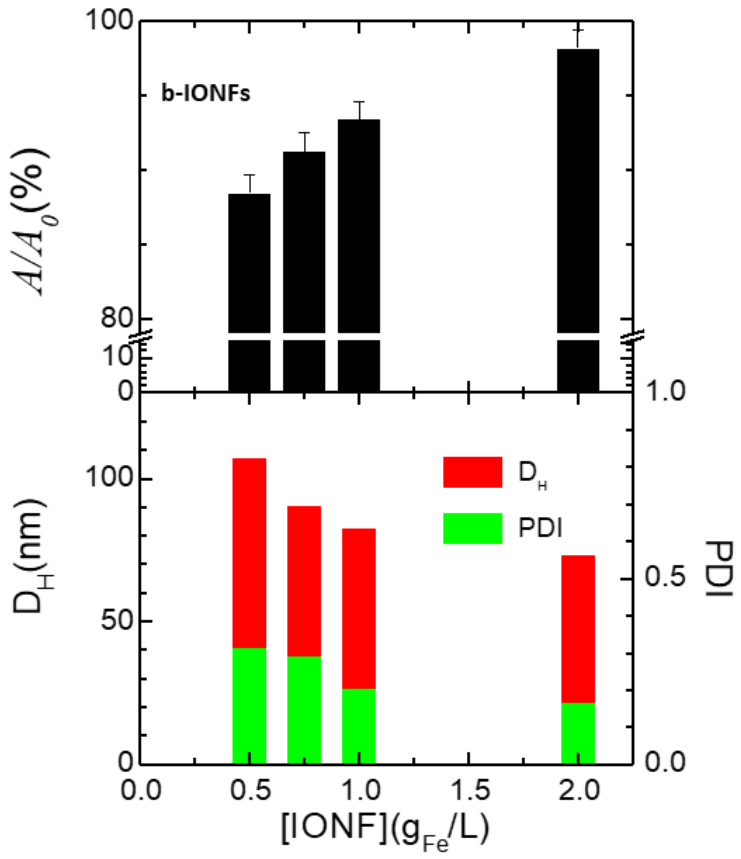

Fig. 5. b-IONF concentration dependence of normalised AC magnetic area (A/A_0), D_H and *PDI* values. Incubation conditions: 0.75 µM divalent analyte concentration and increasing IONF concentrations from 0.5 up to 2 g_{Fe}/L dispersed in 0.1x PB for 1 h at 25°C. AC hysteresis loops were measured at 100 kHz and 24 kA/m.

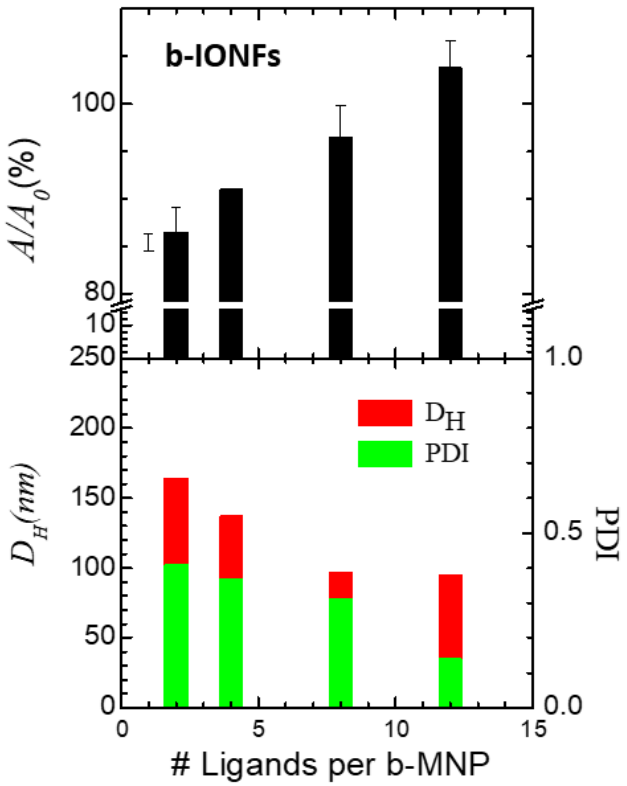

Fig. 6. Normalised hysteresis area (A/A_0), D_H and *PDI* values related to b-IONF conjugated with distinct number of receptors per MNP. Incubation conditions: different b-IONFs receptor formulations at 1 g_{Fe}/L and 1 μM divalent analytes dispersed in 0.1x PB 0 for 1 hour at 25°C. AC hysteresis loops measured at 100 kHz and 24 kA/m.

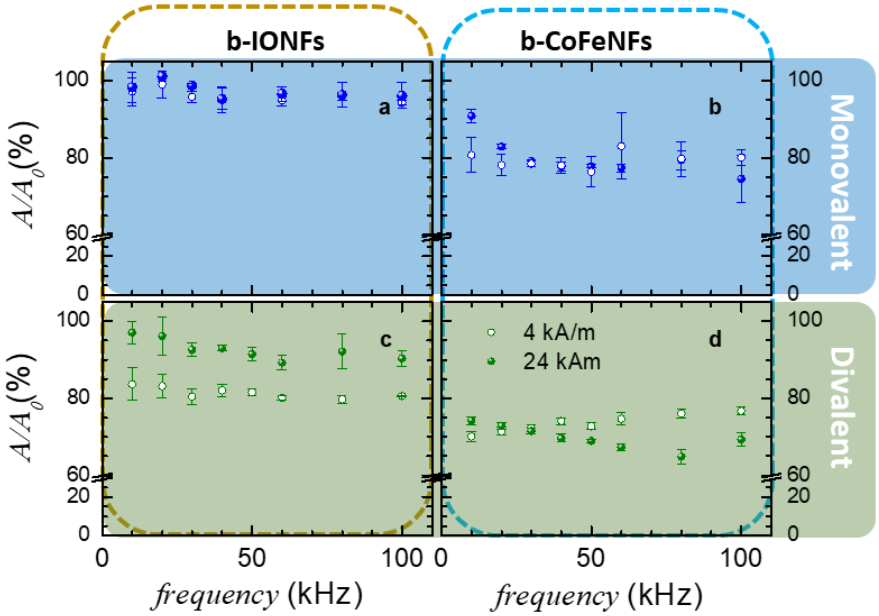

Fig. 7. Frequency dependence of A/A_0 at two field intensities for: a) b-IONFs, and monovalent analyte (blue colour); b) b-CoFeNFs, and monovalent analyte (blue colour);c) b-IONFs, and divalent analyte (green colour); d) b-CoFeNFs, and divalent analyte (green colour). Incubation conditions: b-MNPs ($1g_{Fe+Co}$/L) dispersed in 0.1x PB for 1h at 25°C at 2 μM of monovalent and divalent analytes. Data extracted from **Fig. S6.**